An Examination of the Solar Torsional Oscillation

A THESIS
SUBMITTED TO THE FACULTY OF THE
UNIVERSITY OF MINNESOTA
BY

Cherish Bauer-Reich

IN PARTIAL FULFILLMENT OF THE REQUIREMENTS
FOR THE DEGREE OF
MASTER OF SCIENCE

Dr. Bruce Moskowitz

May, 2017

Acknowledgements

There are several people I would like to thank for their contributions to this thesis. Without their time, effort, and support, I would not have been able to complete this project.

First and foremost, I would like to thank my advisor and committee. In particular, I appreciate the efforts of my advisor, Dr. Bruce Moskowitz, for his willingness to oversee such an unusual topic as well as his patience and support in completing it. Dr. David Kohlstedt was instrumental in enabling me to work on this project. Dr. Kohlstedt and Dr. Max Bezada also served on my committee.

While doing this project, I was employed for some time at North Dakota State University, and several people there also deserve my thanks. In particular, Aaron Reinholz, my supervisor, was flexible and enabled my research efforts both in this project and at work. Dr. Martin Ossowski, Director of the Center for Computationally Assisted Science and Technology, and Dr. Phillip Boudjouk, former Vice President of Research, were instrumental in allowing me access to the computational facilities required for this research.

I would also like to thank Dr. Tamara Rogers of Newcastle University for providing me with the base code which I modified to produce the simulations. I also appreciate her assistance in getting it running.

On a more personal level, there were many friends and family members to whom I am so very grateful: Antoinette Abeyta, Laura Vietti, Yifan Hu, and Cale Anger were dear friends when I was far from home. I am ever appreciative of my wonderful family (Mom, Dad, Mike, Korwynn, and Jacob) for being ever patient with a mom, wife, and daughter who was always slightly distracted and sometimes absent because she was working on yet another degree. I am deeply grateful to and for all of them.

Dedication

This work is dedicated to the memory of Cale Anger, whose life continues to inspire me.

Abstract

Bands of slower and faster flow, known as solar torsional oscillations, are spatially correlated with sunspot appearances on the solar surface. Understanding the relationship between torsional oscillations and sunspots may help to illuminate the conditions of flux tube origination and motion that give rise to the sunspot cycle. This, in turn, may help to understand the process of dipolar magnetic field generation in the sun. In order to better understand the formation and behavior of the torsional oscillation in the presence of convection, magnetohydrodynamic code, with magnetic feedback removed, was used to model the convection zone. In baseline simulations, a fairly consistent signal at the torsional oscillation frequency was detected near the top of the tachocline at mid-latitudes. When a mechanical forcing representing the torsional oscillation was added, it diffused but did not propagate, in contrast to previous works. When the signal varied with latitude, a region of active attenuation was noted at 30° N and S latitudes. These results indicate that specific convection patterns at the top of the tachocline may be responsible for flux tube origination. Further, mechanical forcing alone is insufficient to generate a torsional oscillation in this type of model.

Contents

List of Figures

List of Symbols

A	amplitude of forcing function
$\mathbf{B}$	magnetic flux density
C	co-density
c_p	specific heat at constant pressure
c_v	specific heat at constant volume
$f(r,\theta)$	forcing function distribution
g	gravity
h_ρ	inverse density scale height
h_κ	thermal diffusivity scale height
P	pressure
$\bar{Q}$	reference state heat flux
$R_\odot$	solar radius
r	distance
T	temperature
t	time
$\mathbf{u}$	velocity
U	gravitational potential energy

η	magnetic diffusivity
γ	adiabatic constant
κ	thermal diffusivity
Ω	rotation rate
Ω_{cz}	rotation rate of the convection zone
Ω_{rz}	rotation rate of the radiation zone
Ω'	rotation rate of the convection zone relative to the convection zone
ω_c	torsional oscillation frequency
θ	latitude
ρ	density
ν	viscous diffusivity

Chapter 1

Introduction

1.1 Introduction

The sun does not rotate as a solid body. The outer 30% of the sun, the convection zone, has rotational frequencies of 320 nHz at the poles to 470 nHz at the equator with a generally smooth transition between the two regions. This is commonly referred to as differential rotation. At the radiative interior, the rotation profile becomes constant, with the interior of the sun rotating as a solid body.

The differential rotation does not have a completely smooth transition from equator to poles. There are zones where the velocity is slower or faster than the average. These flows are called torsional oscillations. They were originally discovered by Howard & LaBonte (1980). The velocity differed from a smooth fitted profile by 3 m/s with a faster band on the equatorward side and a slower band on the poleward side of the magnetic activity. Howard and LaBonte stated that these bands took 22 years to travel from the poles to the equator. They also claimed that the velocity amplitude was proportional to sunspot numbers. Because they were measuring surface velocities, they were unable to provide any information about the depth of the flows.

Most current information on torsional oscillations comes from global helioseismology. Global helioseismology uses inversion techniques that are only sensitive to the features that are symmetric about the equator. Information on the meridional flows near the torsional oscillations has therefore been gleaned from local helioseismology. An overview of these studies can be found in Howe et al. (2009).

Several computational models have been developed to better understand the torsional oscillation behavior and origin. One of these studies was performed by Rempel (2007) using a model with implicit convection given by the dynamo equation. This work evaluated thermal and mechanical forcing in order to determine what role each may play in the generation and propagation of the torsional oscillation. In this model, mechanical forcing could create a signal resembling the torsional oscillation that propagated independently toward the poles while thermal forcing was required for motion toward the equator.

This work examines mechanical forcing in an axisymmetric magnetohydrodynamic model with explicit convection and without magnetic feedback. The goal is to assess whether the model dynamics have any impact on mechanical forcing and how these may affect the conclusion that mechanical forcing is a viable means of generating a torsional oscillation under certain conditions.

1.2 Outline

Helioseismology has been used to infer much about the internal structure of the sun and specifically to characterize the behavior of the solar torsional oscillation. These studies show much about the behavior of the oscillation as well as it's spatial correlation to sunspot activity, but they are limited in inferring whether there is a cause-and-effect relationship to temporal correlations between the presence of the two phenomena. Computational models, like the one used in this project, are more useful in attempting to determine the nature of the relationship. Chapter Two will discuss the relevant background information to provide context for the current work.

Chapter Three will discuss both the computational methods of generating the data used for this work as well as the methods of analysis.

The computational model, because it solves convection explicitly, produces data that are inherently very noisy due to the variation in the size of flow structures. This made it necessary to run a simulation without an injected signal (often referred to throughout the work as a perturbation) to determine what behavior was as a result of signal injection and what was naturally occurring in the simulation. Chapter Four presents the results of those baseline simulations.

Chapter Five covers determination of the minimum perturbation required for detection. A difference of means statistical test was used to compare results from the baseline data (shown in

Chapter Four) and varying levels of perturbation strength at three different latitudes.

The behavior of the perturbation as a stationary oscillation is presented in Chapter Six. In another set of simulations, the signal is moved either poleward or equatorward from 45° N and S. The results of the moving oscillation are presented in Chapter Seven.

Finally, Chapter 8 summarizes the major findings of this work. It also presents topics for further inquiry.

Chapter 2

Background

2.1 Helioseismology

The Global Oscillations Network Group (GONG) began accumulating helioseismic data in 1995, and the launch of the Solar and Heliospheric Observatory (SOHO), carrying the Michelson Doppler Imager (MDI), occurred in 1996. This has increased accuracy of observational data, enabling better determination of behavior within the convection zone. The following studies use results from either GONG or MDI, or, in some cases, both.

In 2002, Vorontsov et al. (2002) used five-minute acoustic oscillations to examine velocity changes with an eleven year period. They determined that there were two torsional oscillations - one branch that moved toward the equator and one that moved toward the poles. The poleward oscillation started at 60°, while the equatorward branch began around 30°. The poleward branch was believed to penetrate through the entire convection zone, while the equatorward branch reached to a depth of 1/3 of the convection zone, or 8-10% of the solar radius. However, toward the base of the convection zone at the same latitude, there appeared to be another variation in velocity. The authors indicated that the lack of a variation throughout the convection zone may be a result of noise. The oscillation frequencies were around 5 nHz greater or less than the total rotational frequency of 450 nHz.

Additionally, the phase of the equatorward branch was examined. The phase of the poleward branch could not be assessed. The authors state that, at the surface, both branches start with a zero phase at 42°. The equatorward branch at the surface goes through a phase change of 3π between the zero phase and the equator. In the deeper layers, the phase change is π. The

equatorward branch from one hemisphere, when it meets the equatorward branch from the other hemisphere, has a phase difference of π. Because the phase is not arbitrary between the opposite hemispheres, the authors state that this is indicative of torsional oscillations as a global phenomena.

Finally, the authors indicate that their analysis indicates the presence of a third harmonic. This implies that there is contribution from another harmonic or that the cycle period is not exactly 11 years.

Basu & Antia (2002) place the transition point between high and low branches of the torsional oscillations around 50°. They also state that, at low latitudes, the pattern travels radially outward at a rate of 1 m/s. At higher latitudes, there is either no clear pattern or the oscillation decreases with radius over time. However, the authors note that some of these patterns may not be clear as they did not have data for a complete solar cycle. Like Vorontsov et. al, they also find a contribution from the third harmonic.

Howe et al. (2005) indicate that the oscillation beginning in 2003 originates at about 35-40°. They state that the flows have a phase shift relative to the bottom of the convection zone. They also state that the regions of faster rotation, at lower latitudes, are tilted relative to the equatorial plane. This implies that at the lowest latitudes, the penetration of the flow into the convection zone will be more shallow, on the order of $0.1R_{\odot}$. The phase of the surface expression is lagging the deeper regions by about two years, a time scale much longer than magnetic fields rising through the convection zone but on par with meridional circulation. They also state that, "It should be pointed out that it is not necessarily the case that a pattern propagation of excess rotational speed in a spacetime slice corresponds to the migration of any physical entity."

The authors also examined the periodicity of the signal. They attempted to fit the data to periods of both 11 years and 10.2 years, based on data suggesting this may be closer to the actual period. They found that, for both cases, results at low latitudes at 95% of the solar radius were improved by using a second harmonic rather than a third.

Howe et al. (2006) attempt to quantify how much can actually be inferred about torsional oscillations from global helioseismology. Specifically, they examine differences in two inversion methods, regularized least squares (RLS) and optimally localized averaging (OLA), on data generated from a computational dynamo model. The model used Rempel's nonkinematic dynamo which uses Lorentz force feedback on differential rotation for one case, which generates the poleward zonal flow. The second case incorporates thermal forcing to create the equatorward

flow.

The authors first discussed the accuracy of inversions on phase and amplitude variations. They determined that amplitude tends to be underestimated and cannot be accurately determined below $0.75R_{\odot}$. The phase, however, can be accurately determined, although there is some distortion at high latitudes. Overall, they felt that OLA provided a better reproduction of the phase information at high latitudes. However, it did not resolve amplitude changes as well. The authors felt, however, that these methods could be used to generate a reasonably clear picture of what is happening in the convection zone.

They also noted that none of the inversion results matched those seen observationally. While they state that it wasn't the point of the paper, it does indicate that some other mechanism may be affecting both the torsional oscillation and the magnetic cycle.

Howe (2009) notes that there are additional issues to consider:

- The appearance of the pattern is dependent on the analysis performed. That is, some authors choose to use an analytical expression which is fitted to the rotation, while others use an mean velocity and solve for residuals.
- The equatorward branch of the oscillation lasts for approximately 18 years while the poleward branch exists for only 9 years.
- The relationship between the torsional oscillation and the magnetic cycle is unclear as the oscillation is present before features of the magnetic cycle are observable. Further, the level of magnetic activity varies considerably from cycle to cycle, while the strength of the torsional oscillation seems to be constant.
- The torsional oscillation is present before sunspots begin to emerge.
- The magnetic activity begins at a higher latitude than the equatorward branch of the torsional oscillation.
- The fractional change in shear, going from the bottom of the convection zone to the top, is greater than the fractional change in velocity.

2.2 Models

Yoshimura (1981) argues that the oscillations are generated by dynamo waves propagating along

isorotation surfaces. As the waves build up, they trigger the torsional oscillation, which, in turn, generates cyclic magnetic activity.

The approach is to solve the dynamo equation using a mean field model. The form of the velocity is defined: average velocity field is differential rotation, and the torsional oscillation is included in the form of a velocity perturbation. The non-linear component to the perturbation is assumed to be small enough that the linear effects will dominate.

Yoshimura examines the Lorentz field generated by the perturbation, which consists of the Lorentz force and a viscous term to represent small-scale turbulence. The waves generated by the Lorentz force originate near the base of the convection zone and propagate upward along isorotation surfaces. The pattern begins near the pole and travels equatorward with a periodicity of 11 years. Yoshimura states that the waves will appear when they encounter an upper surface boundary and are deformed.

Because the appearance occurs with interaction of the waves with the upper boundary, the boundary conditions are examined. The oscillatory component of the solution does not change by altering the boundary conditions. However, the viscous term of the perturbation changes the phase relationship between the torsional oscillation and the magnetic activity as the boundary conditions are altered. Yoshimura concludes that open boundary conditions are appropriate at the top of the convection zone.

The simulation results presented show different components of the Lorentz force evolving over time. These results compare favorably with Howard and LaBonte's observational results. The only plot of angular velocity describes the differential rotation and thus doesn't provide direct information about the torsional oscillation that this model generates.

Spruit (2002) suggests generation of torsional oscillations is a result of the magnetic field gradient, but that the mechanism is thermal rather than magnetic: the magnetic fields inhibit convection and, on small scales, enhance radiative cooling. He develops a pseudopolytropic model which incorporates a temperature stratification. This also results in a non-constant adiabatic gradient. The resulting perturbation in temperature causes an Ekman layer near the surface, which generates a change in flow velocity.

Spruit's model makes several predictions. First, the flow at the surface must be directed from edges of the main activity belt toward the center. Second, the direction of flow will change with depth. The flows are averaged, but the model suggests that sufficiently large structures with respect to the Ekman layer should have cyclonic circulation. Finally, it predicts that the time for

the effects to propagate to a depth of approximately 100 Mm is about 2 weeks.

Rempel (2007) attempted to validate this model by using a mean field hydrodynamic model that did not include Lorentz forces. In this model, the torsional oscillation was created either using mechanical forcing via a velocity perturbations and thermal forcing via temperature perturbations. He determined that the mechanical forcing was sufficient to create a poleward torsional oscillation but that thermal forcing was required in combination with mechanical forcing to generate an equatorward torsional oscillation. His conclusions were that while Spruit's model does generate some of the surface features of the torsional oscillation, it does not create the correct behaviors and features in the lower half of the convection zone.

Rempel's model uses parameterized convection, as described in Rempel (2005). His mean field approach did not generate the desired characteristics in the lower zone. This prompts the question of whether a different computational approach would also generate a torsional oscillation using this method and, if so, would it change the dynamics present in the lower convection zone. This work attempts to answers those questions, and the method therefore closely follows the approach taken in Rempel (2007).

Chapter 3

Methods

3.1 Simulation

The numerical model used to study the torsional oscillation in this work is a simplified version of that in Rogers (2011). In that work, the full set of axisymmetric MHD equations is given by the following:

$$\nabla\cdot(\bar{\rho}\mathbf{u}) = 0, \tag{3.1}$$

$$\nabla\cdot\mathbf{B} = 0, \tag{3.2}$$

$$\frac{\partial\mathbf{B}}{\partial t} = \nabla\times(\mathbf{u}\times\mathbf{B}) + \eta\nabla^2\mathbf{B}, \tag{3.3}$$

$$\frac{\partial\mathbf{u}}{\partial t} + (\mathbf{u}\cdot\nabla)\mathbf{u} = -\nabla P - C\bar{g}\hat{r} + 2(\mathbf{u}\times\Omega) + \frac{1}{\rho}(\mathbf{J}\times\mathbf{B}) + \nu\left(\nabla^2\mathbf{u} + \frac{1}{3}\nabla(\nabla\cdot\mathbf{u})\right), \tag{3.4}$$

$$\begin{aligned}\frac{\partial T}{\partial t} + (\mathbf{u}\cdot\nabla)T = \quad & -u_r\left(\frac{d\bar{T}}{dr} - (\gamma-1)\bar{T}h_\rho\right) + (\gamma-1)Th_\rho u_r \\ & +\gamma\kappa[\nabla^2 T + (h_\rho + h_\kappa)\frac{\partial T}{\partial r}] + \frac{\bar{Q}}{c_v}.\end{aligned} \tag{3.5}$$

Variables with a bar above them represent the value for the reference state while state variables without a bar represent the deviation from the reference state. Equation 3.1 ensures conservation of mass, with $\bar{\rho}$ as the density and $\mathbf{u}$ as the velocity with components u_r, u_θ, and u_ϕ. Gauss' Law is given in Equation 3.2, and the induction equation is given in Equation 3.3. For this work, the magnetic field was removed from the model to more closely match the conditions in Rempel's model. This means that Gauss' Law (Equation 3.2) and the induction equation (Equation 3.3) are not included in the final model.

The momentum equation is presented in Equation 3.4. Because of the lack of magnetic feedback, the term containing the Lorentz force is eliminated from the equation, which is then reduced to:

$$\frac{\partial \mathbf{u}}{\partial t} + (\mathbf{u}\cdot\nabla)\mathbf{u} = -\nabla P - C\bar{g}\hat{r} + 2(\mathbf{u}\times\Omega) + \nu\left(\nabla^2\mathbf{u} + \frac{1}{3}\nabla(\nabla\cdot\mathbf{u})\right). \tag{3.6}$$

In the momentum equation, g is gravity, Ω is the rotation rate, and ν is the viscous diffusivity. The value C is the co-density and P is the reduced pressure. They are defined in Braginsky & Roberts (1995) and Rogers & Glatzmaier (2005) as:

$$C = -\frac{1}{T}\left(T + \frac{1}{g\bar{\rho}}\frac{d\bar{T}}{dr}p\right), \tag{3.7}$$

and

$$P = \frac{p}{\bar{\rho}} + U. \tag{3.8}$$

The temperature is given by T while p is the deviation of pressure from the reference state and U is the difference between the gravitational potential energy and reference value.

Finally, the temperature equation is given in Equation 3.5. In this equation, γ is the adiabatic index, which is defined as

$$\gamma = \frac{c_p}{c_v}. \tag{3.9}$$

The value of γ is 5/3 in these simulations. In Equation 3.9, c_p is the specific heat at constant pressure, and c_v represents the specific heat at constant volume. The thermal diffusivity is κ while the inverse density and thermal diffusivity scale heights are h_ρ and h_κ, respectively. The term involving $\bar{Q}/c_v$ is used to maintain the steady state temperature gradient but has also been

excluded in this model.

Because the simulation was not 3D, a rotation profile was imposed on the convection zone to approximate helioseismically inferred differential rotation given from Thompson et al. (1996) as

$$\Omega_{cz}(r,\theta) = 456 - 72\cos^2\theta - 42\cos^4\theta \tag{3.10}$$

The value in the tachocline, the transition region between the radiative zone and convection zone, was set to a constant 441 nHz, represented by Ω_{rz}. The difference between the observed rotation outside of the tachocline and the constant was

$$\Omega' = \Omega_{cz} - \Omega_{rz} \tag{3.11}$$

This term was added to the azimuthal component of the momentum equation.

3.1.1 Baseline

The first set of simulations was performed as a control case. In this set of simulations, the model was run for approximately 50 torsional oscillation periods. The results were used to characterize the solar convective behavior at the solar torsional oscillation frequency without a perturbation or with any magnetic feedback. They were also used to contrast with the presence of a perturbation in later simulations.

3.1.2 Stationary Torsional Oscillation

These simulations included three stationary perturbations which follow the design laid out in Rempel (2007). The simulations incorporated a velocity perturbation placed in the convection zone for mechanical forcing. The form of the perturbation is

$$A\Omega' f(r,\theta)\sin(\omega_c t), \tag{3.12}$$

and it was added to the azimuthal component of 3.6. A is a multiplier chosen to adjust the amplitude of the perturbation. The distribution is given by

$$f(r,\theta) = exp\left[-\left(\frac{r - r_o}{\Delta r}\right)^2 \right] exp\left[-\left(\frac{\theta - \theta_o}{\Delta \theta}\right)^2 \right]. \quad (3.13)$$

The perturbation center, given by θ_o, was placed at latitudes of 30°, 45°, and 60° in both northern and southern hemispheres with a latitudinal extent of $\Delta\theta = 0.125$. The radial values are $r_o = 0.85R_\odot$ and $\Delta r = 0.05R_\odot$. The period in Equation 3.12 was 11 years so the frequency was approximately 2.9 nHz, corresponding to ω_c of $18.2 \cdot 10^{-9}$ rad/s.

One of the first objectives was to determine the minimum strength necessary for the perturbation to be detected. At each latitude, perturbations with amplitudes (A) of 0.01, 0.001, and 0.0001 of Ω' were simulated. With a 1% perturbation ($A = 0.01$), the proportion of Ω was approximately 0.15% at 60°, 0.06% at 45°, and 0.001% at 30°. The simulation became unstable at the high and middle latitude at $A = 0.05\Omega'$ and low latitude at $A = 0.10\Omega'$.

3.1.3 Moving Torsional Oscillation

There were two simulations used to evaluate the effect of motion on the torsional oscillation. Both simulations used a constant value of 0.1% ($A = 0.001$) of the differential rotation evaluated at $r_o = 0.85R_\odot$ and 45° N and S. The perturbation did not oscillate in magnitude, as in the stationary cases but traveled along a constant radius. One simulation modeled the perturbation traveling poleward from 45° N and S to 84° N and S. The other simulated perturbation traveled equatorward from 45° N and S to 6° N and S. The period of travel was 11 years.

3.2 Spectral Evaluation

The analyses of the resulting data were performed using the multi-taper spectral method. This method, developed by Thomson (1982), involves windowing an entire time-series using a set of orthogonal functions. Windowing the function reduces spectral leakage while using tapers creates multiple realizations, reducing the variance of the estimate. Bronez (1992) shows that Thomson's multi-taper spectral method has a 10-20 dB improvement in estimates relative to the Welch method of weighted overlapping segment averaging. The multi-taper method also works well when data range over several decibels, which makes it appropriate for working with the red power spectra that result from solar velocities, particularly near the base of the convection zone.

Prieto et al. (2009) implemented the multi-taper spectral method using Fortran. As implemented in this work, the method evaluated the velocity time-series independently at each grid point. Therefore, the spectral results have no dependence on adjacent grid points beyond the initial production of the data. This also means that, unlike analysis of spherical harmonics, there is no requirement for symmetry about the equator.

The spectral analyses shown in the following chapters were of three types. The short-length analyses used 2000 data points covering approximately 2.3 torsional oscillation periods. These were performed on all simulations (Chapters 4, 6, and 7) to give an indication if there were temporal changes in the spectral behavior. The results of the simulations have been averaged to provide the results in Chapters 6 and 7.

Two longer length analyses were performed on the baseline case (Chapter 4). The long-length analysis was performed over 18.4 cycles of the torsional oscillation. The other was performed on approximately 25 cycles (approximately half the data set) using a reduced sampling rate.

The short- and mid-length analyses used 9 tapers to provide both sufficient smoothing while minimizing the variance while the longest analysis used 5 tapers.

The flow chart shown in 3.1 shows the process used to develop the spectral power maps shown in the following chapters.

3.3 Statistical comparison

In order to evaluate where the perturbation was detectable in the low-amplitude stationary cases, a hypothesis test using difference of means was utilized as a comparison between average of the control simulation with no perturbation and the other simulations. Each latitudinal zone was evaluated separately using the maps produced by the short-range spectra. The power at 2.9 nHz was averaged for all radial values across a latitudinal zone. Because the 1% and baseline models had multiple short spectra, a single mean across all simulation results was computed rather than taking a mean of individual short spectral means. Then the base-10 logarithm of each mean was computed. The logarithm of the mean was the value compared to the baseline population value mean, which was also a logarithm.

A hypothesis test was performed using the difference in means, the baseline mean minus the perturbation mean, with a 95% confidence interval. When the mean from the baseline data is smaller than the perturbation, the result is a negative value.

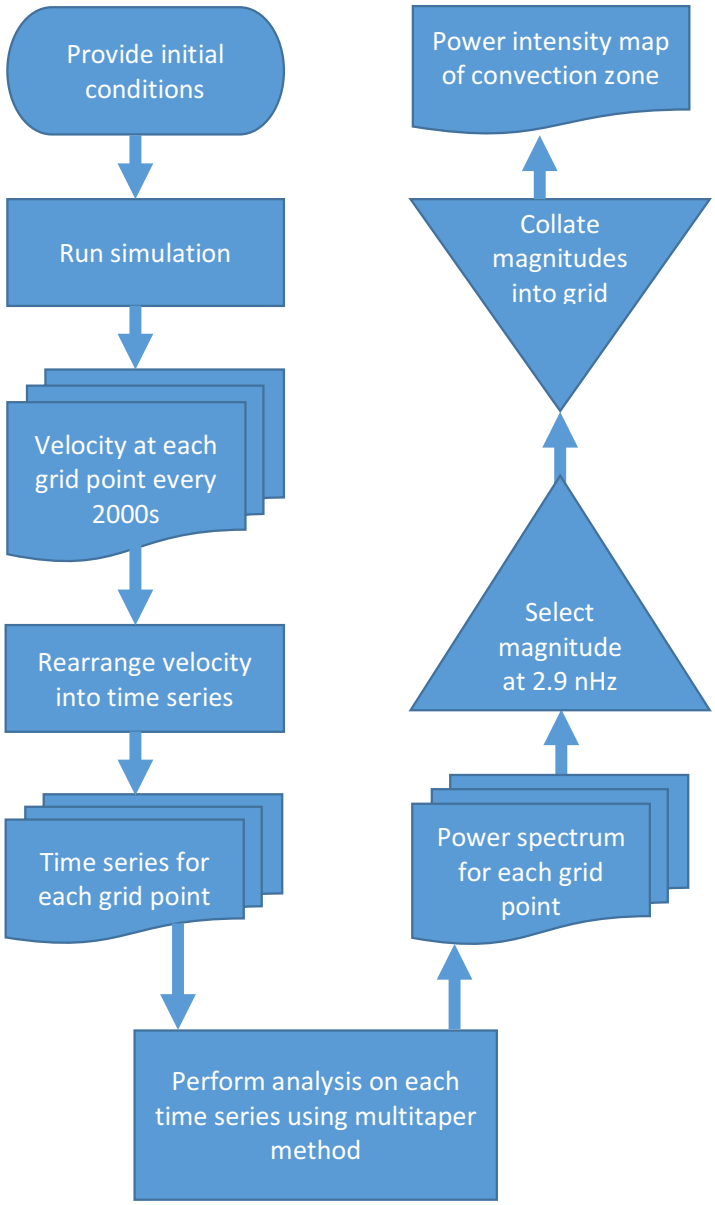

Figure 3.1: Explanation of process used to create power maps

If the confidence interval giving the range of the differences in means includes zero, we can conclude that there is not sufficient evidence to assume any difference between the mean energy of the system where no forcing is occurring and where it is occurring. If, however, the interval does not include zero, we can be 95% confident that the means will not be the same for that particular latitude.

Chapter 4

Baseline Model Analysis

4.1 Overview

This chapter examines the behavior of the convection zone at the torsional oscillation frequency without magnetic feedback and without a forcing to represent the torsional oscillation. The model was run in order to create baseline data with which to compare later simulations that do include a forcing. The primary result obtained was that these conditions allow for generation of a signal at the top of the tachocline near 45°. There is often weaker frequency content at the same latitude but closer to the center of the convection zone. It is not clear whether this represents radial propagation of the signal near the tachocline or is independent of it, but its magnitude and expanse seem to be correlated strongly with the same characteristics of the tachocline signal. There are also cells on the equatorward side of the signal in both hemispheres. It is not clear if these cells are a result of the signals at 45° or if conditions are favorable to generate these cells independently. Finally, the appearance of these cells may have a long term periodicity.

4.2 Results

We begin by examining the model behavior at the 11-year period without an added perturbation. The frequency distribution from the high resolution results covering 23 cycles is shown in 4.1, which is a series of frequency maps showing results from short-length analyses. Each crescent represents the analysis of an adjacent, non-overlapping time series with a span of 2.3 sunspot cycles. The total timespan represents 27.6 cycles of 11 years for a total of 303.6 years. All

maps use the same relative color scale where white represents the largest values, followed by red, then progressing along a rainbow scale to the smallest values at purple with black being the minimum.

Activity is present near the base of the convection zone at 45° in each hemisphere in nearly all maps even though the intensity is not constant. The behavior at other latitudes varies through the progression. The activity poleward of 45° is minimal except in the second to last map. Equatorward of the active region, there is little activity initially before becoming consistently active in the center of the progression and then finally waning again. There is also radial stratification displayed in the map: the outer fourth of the convection zone is inactive during the entire progression.

The linear and logarithmic representations of the spectral energy data from the average of the progression are shown in 4.2 on a linear scale and 4.3 on a logarithmic scale. There is useful information that can be gleaned from both representations. In both maps, the top of the tachocline is represented by a white arc.

One of the most obvious features in both maps is the radial stratification. The linear map, like the progression in 4.1, shows very little frequency content outside of cells in the bottom two-thirds of the convection zone. This gives the erroneous impression that there is no activity outside of that band, whereas one can see that, on the logarithmic map in 4.3, there is some activity but it is attenuated significantly in the top quarter of the convection zone.

The linear plot in Figure 4.2 is useful for identifying active regions. In particular, one first notices that the frequency content has a strong dependence on latitude. The activity in the region from 30° N and to 30° S is concentrated in individual, relatively weak cells that are confined to the lower half of the convection zone.

In latitudes poleward from 30°, activity appears in radial levels along the top of the tachocline and in the center of the convection zone. The region between 30° poleward to 60° in both hemispheres is generally the most active, with the most intense activity along the top of the tachocline. This is connected to another band of activity which may be radial propagation of the signal from the active region.

Finally, the regions from 60° poleward show higher levels of activity at the top of the tachocline while the middle two-thirds of the convection zone has a lesser but more spatially consistent level of activity.

The logarithmic representation is shown in 4.3. The only noticeable difference in latitudinal

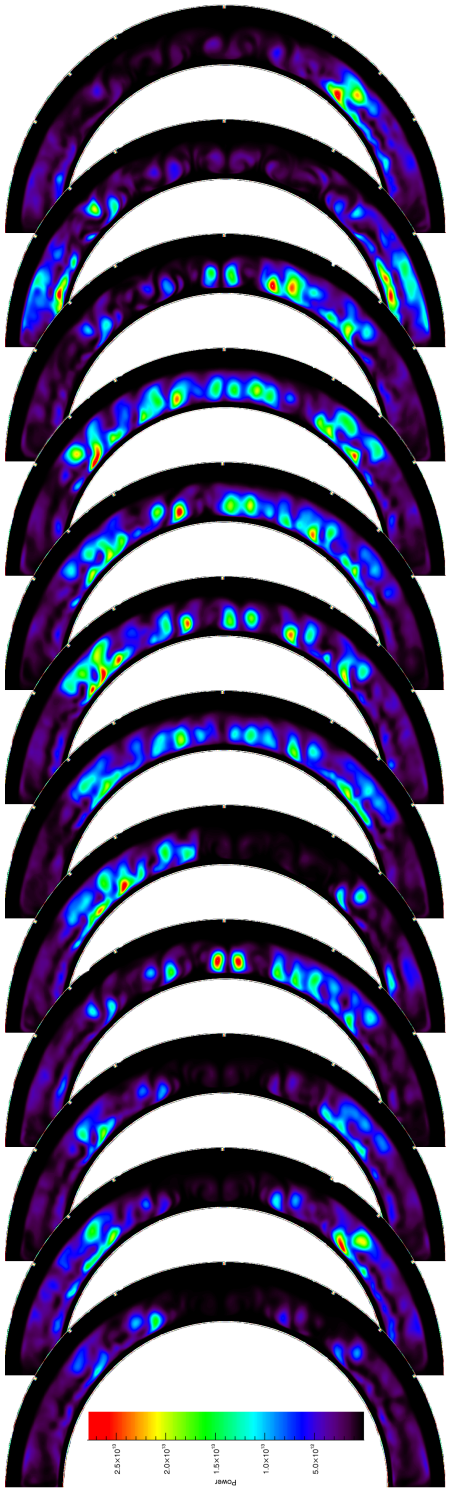

Figure 4.1: Progression of torsional oscillation frequency without forcing

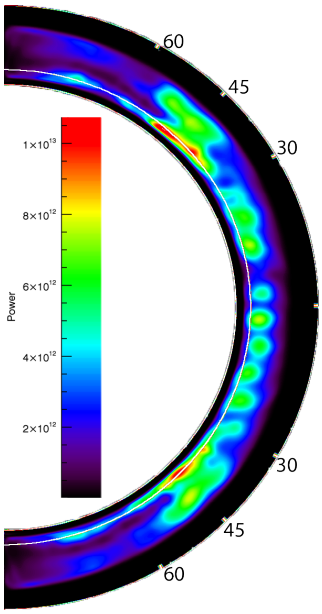

Figure 4.2: Linear scaling of averaged spectra without perturbation

variation occurs near 45° in each hemisphere, where the spectral power peaks inside the top of the tachocline. As mentioned before, the radial stratification is very obvious and homogenous. One difference from the averaged plot is that there is a thin band of higher activity beneath the signal maximum near the bottom of the tachocline as well as near the poles.

A long-range spectral analysis was performed over 11.5 cycles, focusing on the first half the progression. The linear map of this analysis is shown in 4.4 while the logarithmic plot is 4.5.

There are some differences between these results and the average. First, most of the activity in the linear plot is not as strong relative to the signal present at latitudes near 45°. There is more activity outside of this region in the averaged plot. While the equatorward activity is still noticeable, the poleward activity is much smaller. Second, the logarithmic map shows more variation in activity with apparent drops in energy along certain paths through the convection zone, often beginning in the tachocline. Again, the activity lower in the tachocline beneath the maximum can be observed in this map.

The spectral map shown in Figure 4.6 is a result of using a decimated signal (sampled at 1/50th the rate of the previous signals) over a period of 10 cycles or 110 years. There was no filtering performed on the signal. The resulting map likely suffers from some level of aliasing

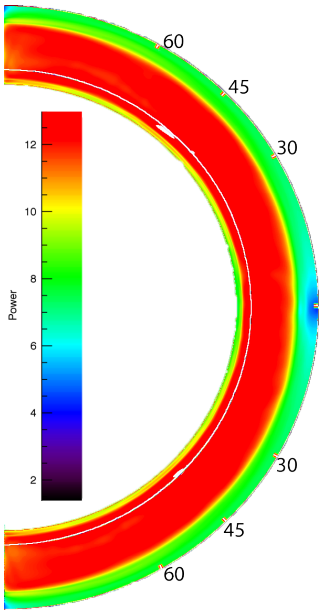

Figure 4.3: Logarithmic scaling of averaged spectra without perturbation

but is a more refined view of this frequency due to the longer overall period resulting in much higher resolution spectra. Unlike previous maps, the red arc inside the plot indicates the base of the tachocline and the portion below being the outermost portion of the radiative zone. The white line, like other maps, represents the top of the tachocline.

The map does not show the radial stratification present in the other maps. This may be a result of the longer period contributing more but also may be a result of aliasing of higher frequencies due to lack of filtering. The strongest signals are still somewhat restricted to lower and mid-radial-level bands.

There are significant pockets of lower activity that are also not seen in the other plots resulting a high level of symmetry between the hemispheres. It is notable that while there are still high levels of activity near top of the tachocline at 45°, there is a pocket of lower activity directly poleward. There is also an area of reduced activity directly equatorward at 30°. This coincides with a feature from the radiative zone as well as a pocket of reduced activity at the outermost portion of the convection zone.

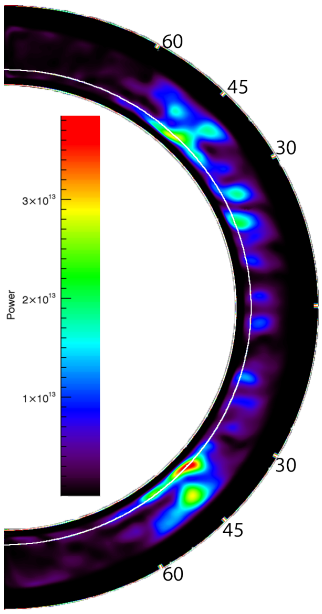

Figure 4.4: Linear scaling of long-range spectra without perturbation

4.3 Discussion

These results indicate several things about this model. First, and likely most significant, is that there is a naturally occurring oscillation that has the same frequency and origination point as the torsional oscillation. The frequency distribution indicates that propagation of this particular frequency is attenuated in the outer quarter of the convection zone but does occur in the lower three-quarters. Activity is generally strongest near the top of the tachocline at all latitudes but is somewhat suppressed at mid-depth except nearest the middle latitudes in each hemisphere.

This points to the possibility that the torsional oscillation may be a natural result of interaction of non-magnetic forces operating at the top of the tachocline. It is not clear if this signal has vorticity and could be involved in flux tube generation or if it is simply an oscillation in the azimuthal velocity, however. Therefore, it cannot be determined what the exact relationship is between the signal and torsional oscillation.

Some inferences about the observed behavior can be made from data presented on the non-magnetic model in Rogers (2011). The meridional velocity structure is shown in 4.7. In this figure, the red represents flow toward the south pole while blue is toward the north pole. First,

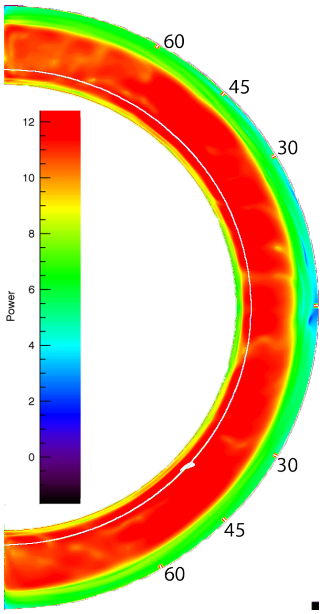

Figure 4.5: Logarithmic scaling of long-range spectra without perturbation

the meridional velocity structure observed at high latitudes, seems to resemble a single cell of meridional circulation with surface flows poleward and inner flows equatorward. There are exceptions, though, such as at very top of the convection zone. At the base of the convection zone near the poles, there are counter-rotating cells. Other similar but smaller counter-rotating cells appear at the tachocline from mid-latitudes toward the equator. These may be actual individual cells, or they may be weakened forms of a large scale cells that resemble the double-celled meridional flow discovered in Zhao et al. (2013).

Equatorward of the strong signal, the flow near the base of the convection zone is primarily equatorward but with a narrower radial structure than the return flow. This would seem to match the appearance of the individual cells that seem to form at low latitudes.

The azimuthal flow is shown in 4.8. In this plot, the outer white line represents the base of the convection zone and the inner white line represents the base of the tachocline. The red represents positive values relative to the mean differential rotation value of 441 nHz. The blue represents negative values relative to the mean. Of particular note is that most values poleward of 30° are negative to neutral. At approximately 45° at the top of the tachocline in both hemispheres, there is a relatively strong positive flow located just below a negative flow at the base of the convection

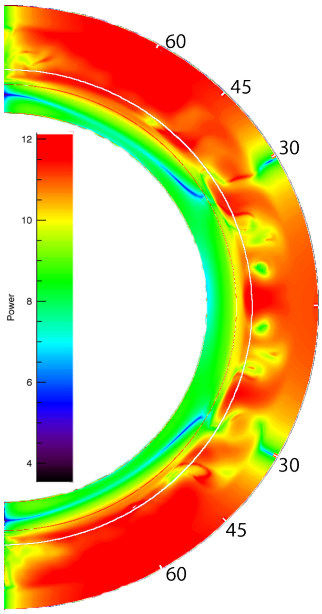

Figure 4.6: Very long spectra with decimated signal

zone.

Forces near the top of the tachocline are shown in Figure 4.9. In these plots, the dashed line represents the Coriolis force and the dotted line represents the Reynolds stress. The plots also show two solid lines, one representing the total force and the other representing diffusion terms. The solid line with the larger magnitude represents the force while the smaller is the diffusion.

These plots show that, at the top of the tachocline ($0.71R_{\odot}$), the Reynolds stresses, Coriolis force, and diffusion all approach zero near 45°. Equatorward of this latitude, the Reynolds stress dominates while the Coriolis force is larger on the poleward side. In the plots at lower depth, the Coriolis force seems to switch direction in the poleward latitudes. This could contribute to the generation of the oscillation as it indicates that there may be some shearing, although it is not clear if there is a periodicity to this behavior given the values are averages. However, the force distributions do not seem to have the same angular distribution as the signal, so it's not clear why this would affect signal generation in that particular location but not at other latitudes.

The signal following the top of the tachocline could potentially be as a result of counter-rotational cell in that area, carrying the oscillation with it. Likewise, the poleward flow in the center radial region of the convection zone would potentially carry or generate a pseudo-periodic

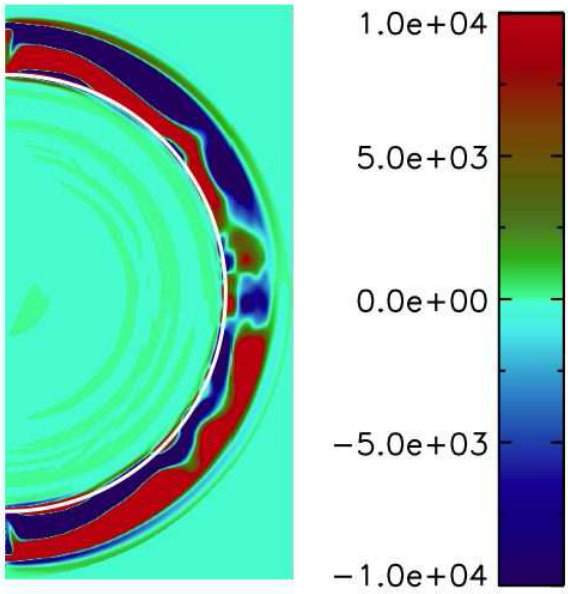

Figure 4.7: Velocity profile excerpted from Rogers (2011)

signal. This flow structure is disrupted near 45°, which corresponds to the strongest signal area.

Looking at the simulation results on a longer time scale, it is clear that while the location at the base of the convection zone that has the highest level of activity is present in most of the simluations, it is not active during the duration of the entire time series. Near the beginning and end of the progression shown in Figure 4.1, there are periods with minimal activity at 45° and equatorward. At the end of the progression, activity is noted at the poles which isn't present throughout the rest of the sequence while most of the remainder of the disk is inactive.

The time progression gives the impression that there could potentially be a periodicity to the behavior, but this would be very long term with a period potentially on the order of 120-140 years. The model was not run long enough to provide sufficient resolution to determine if there was a periodicity in that range. If there is a relationship between the signal and torsional oscillation, however, this time period could coincide with behavior such as grand minima.

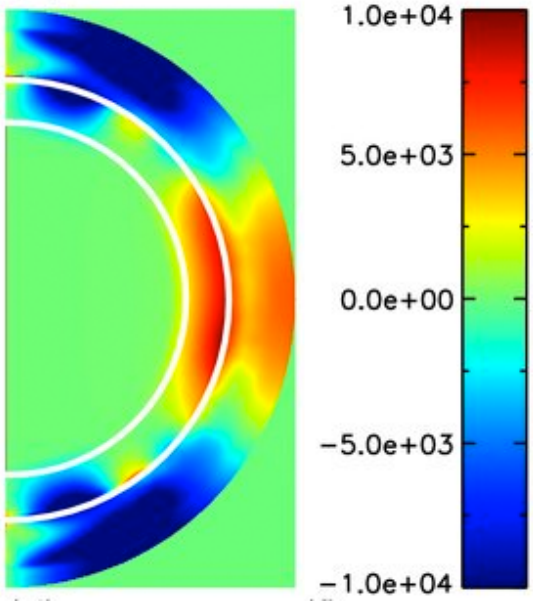

Figure 4.8: Forces at the tachocline excerpted from Rogers (2011)

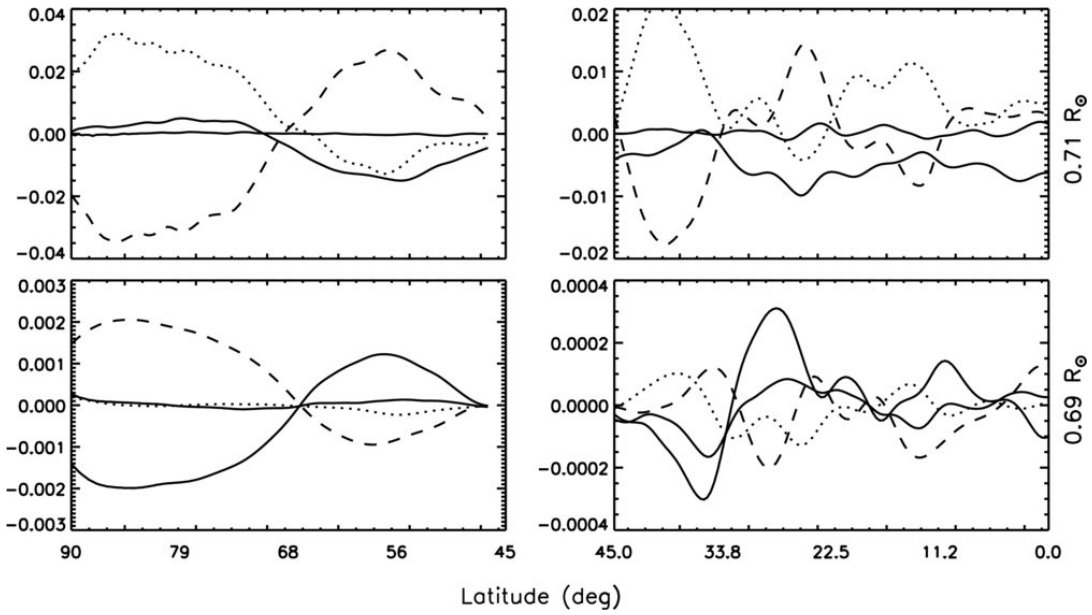

Figure 4.9: Forces at the tachocline excerpted from Rogers (2011)

Chapter 5

Stationary Oscillation Minima

5.1 Overview

As there are already naturally occurring signals present near the latitudes where the perturbation would be introduced, it is necessary to determine the minimum signal amplitude required for detection of the imposed signal. It was determined that a minimum signal size of 0.001% of Ω was necessary for detection of the imposed signal. This value is considerably less than the value used in models using parameterized convection. Further, this input corresponded to an increase in average latitudinal power approximately an order of magnitude greater than the ambient power level.

5.2 Control

As discussed in Chapter 3, a difference of means test was used to definitively determine the presence of the perturbations. The 95% upper and lower confidence levels for the difference of means were computed for each latitude level of the simulation. In the figures that will follow, the confidence interval is shown in cyan. If the difference in means was not significant at this level, then zero would be included in that range. If the baseline data was greater, then the lower confidence level boundary would be greater than zero. Conversely, if the sample was greater than the baseline data, the upper confidence level boundary would be below zero.

Before examining the stationary perturbations, it should be noted that it is not uncommon for samples without forcing to have some latitudes where the difference in means did not equal

zero. Figure 5.1 is an ideal case where the sample, taken from the middle of the progression (sixth slice) shown in the previous chapter, has a mean difference that is not noticeably different from the average for the entire simulation.

Figure 5.2 and Figure 5.3 show two examples of subsets of data where the means do differ. Figure 5.2 shows a region from approximately 35° N to the equator where the average of the baseline simulations had a mean that exceeded the sample by about 1 dB. Figure 5.3 shows that the baseline data exceeded the sample except toward the poles.

The comparison of samples to the baseline data showed that when differences did exist between the sample and baseline, the baseline data was almost always greater with the upper confidence level of the range no greater than 2 dB.

5.3 Low-Latitude Results

The approximate distribution of the low latitude perturbation is shown in Figure 5.4. As can be seen, the perturbation is centered at 30° N and 30° S. The extent of the perturbation is from 15° up to 45° in each hemisphere and occupies the upper 2/3 of the convection zone.

At all latitudes, there was first an examination to determine a minimal level at which the torsional oscillation could be detected. In Figure 5.5, baseline simulation mean is larger than the perturbation simulation mean from approximately 10° N to 15° S as well as around 30° N. This is within the range seen when there was no forcing. However, there are no regions where the perturbation simulation data means exceed the baseline data, so the perturbation is not detectable at this level. Similar observations can be made in the case of 0.1% forcing, shown in Figure 5.6.

When the perturbation magnitude is increased to 1%, there is a very obvious difference in the means. A very narrow perturbation is easily detected that has a magnitude that is approximately one order of magnitude greater than the baseline data. However, the meridional extent of the detectable perturbation is only about 10° in either hemisphere.

5.4 Mid-Latitude Results

The mid-latitude perturbation in Figure 5.8 is centered at 45° N and 45° S. The extent of the perturbation is from 30° to 60° in each hemisphere. As before, it occupies the upper 2/3 of the convection zone.

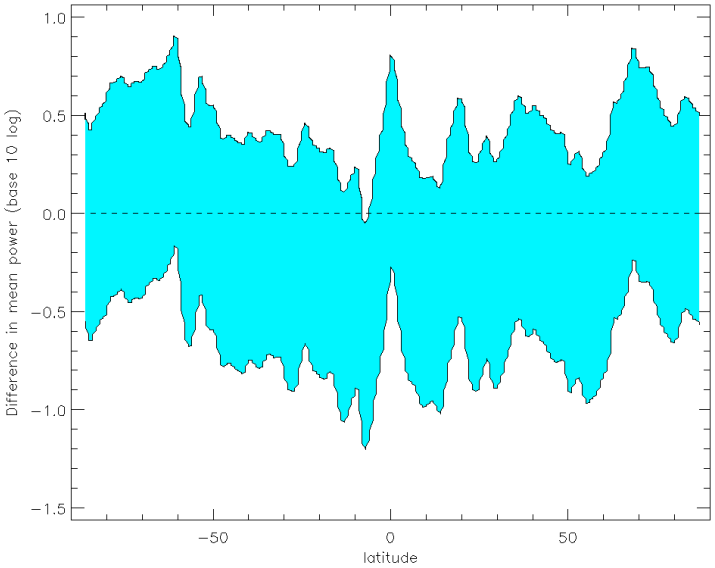

Figure 5.1: Difference of means between sixth mid-simulation sample and average for simulation

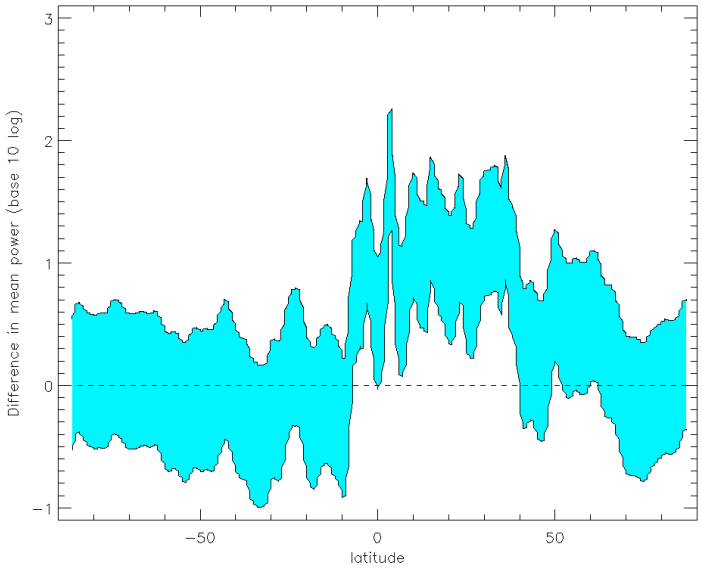

Figure 5.2: Difference of means between fifth mid-simulation sample and average for simulation

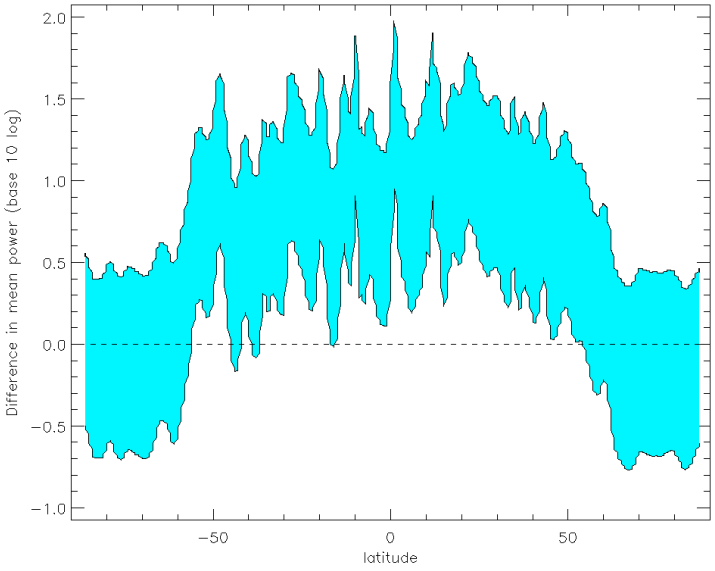

Figure 5.3: Difference of means between eleventh mid-simulation sample and average for simulation

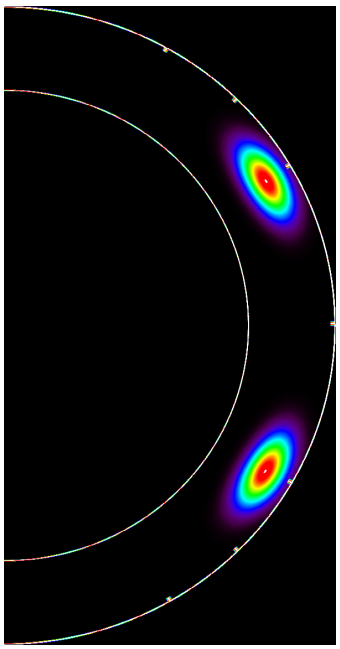

Figure 5.4: Low-latitude torsional oscillation distribution

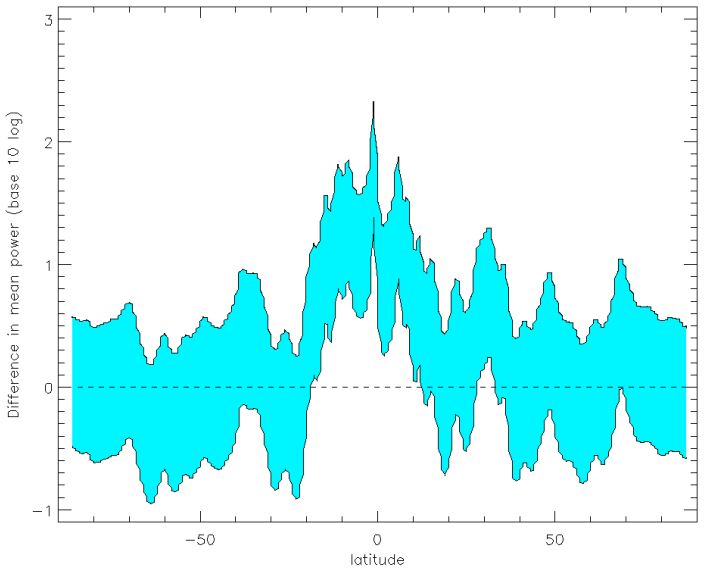

Figure 5.5: Low-latitude forcing with 0.01% of Ω'

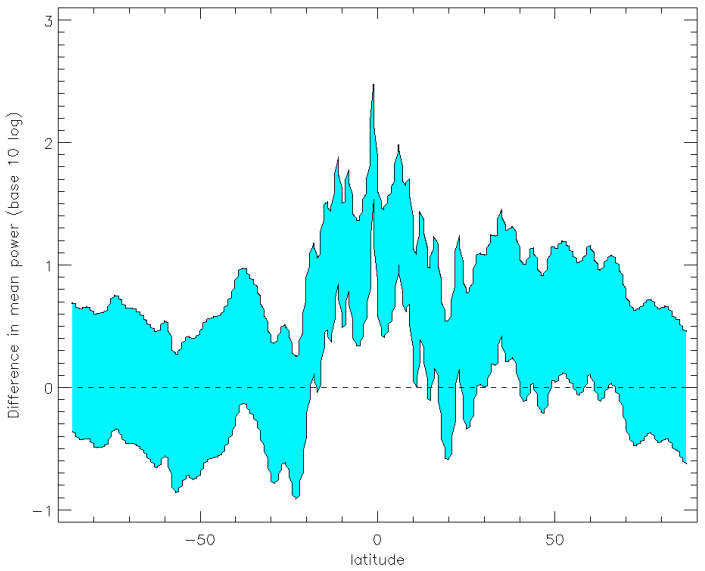

Figure 5.6: Low-latitude forcing with 0.1% of Ω'

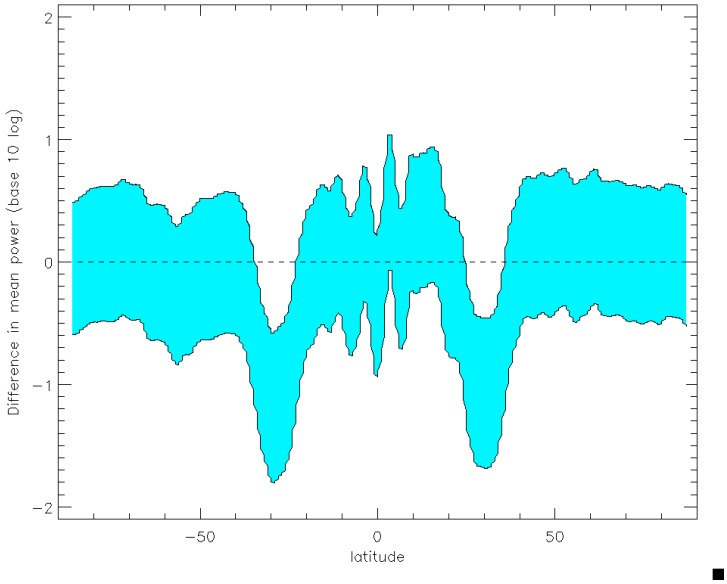

Figure 5.7: Low-latitude forcing with 1% of Ω′

Like the low-latitude perturbation, the perturbation cannot be detected with an amplitude of 0.01%, as can be seen in Figure 5.9. Additionally, it also has peaks near the center and near 30° N where the baseline data actually exceeds the simulation with the perturbation. When the amplitude of the perturbation is increased to 0.1%, it is easily seen in Figure 5.10 with a meridional span of approximately 20° in each hemisphere. The results indicate that the perturbation signal is approximately two orders of magnitude larger than the baseline data.

5.5 High-Latitude Results

The high-latitude perturbation in Figure 5.12 is centered at 60° N and 60° S. The extent of the perturbation is from 45° to 75° in each hemisphere. The radial extent is the upper 2/3 of the convection zone.

Unlike the perturbation at other latitudes, this one is easily detectable in Figure 5.13 even at an amplitude of 0.01%. The center portion of the difference indicates that the baseline data is still greater near the equator and in both hemispheres near 30-40°. The width of the perturbation is only about 10°.

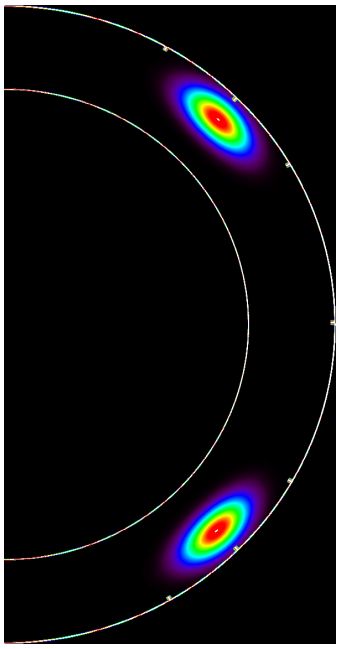

Figure 5.8: Mid-latitude torsional oscillation distribution

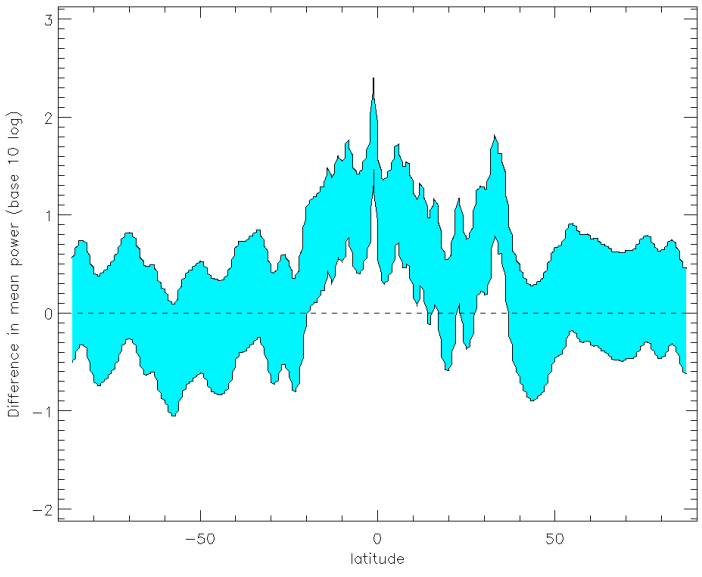

Figure 5.9: Mid-latitude forcing with 0.01% of Ω'

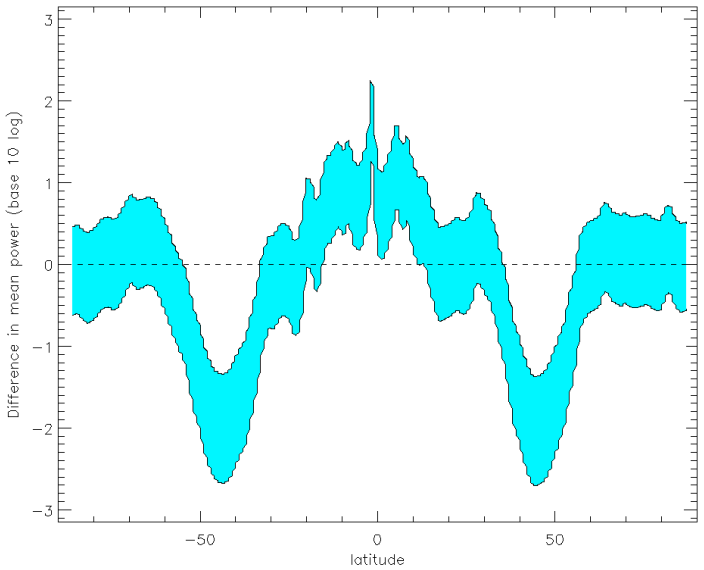

Figure 5.10: Mid-latitude forcing with 0.1% of Ω'

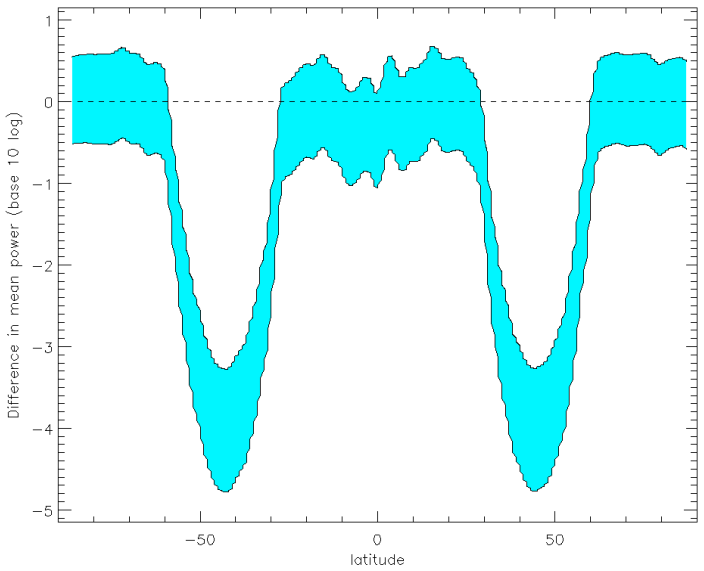

Figure 5.11: Mid-latitude forcing with 1% of Ω'

The plots for the 0.1% perturbation in Figure 5.14 and 1% perturbation in Figure 5.15 closely resemble their mid-latitude counterparts in both angular width and magnitude.

5.6 Discussion

The smaller amplitude (0.01% and 0.1%) perturbations generally showed more differences with the baseline data, particularly toward the equator, than the 1% perturbations. The reason for this is that the comparison at low amplitudes was with a significantly smaller data set than with the 1% simulations. The data sets for the 1% simulations were 10 times as large, reducing the variance at lower latitudes resulting in a better fit.

The ability to detect low-amplitude perturbations depends on latitude. It is obviously easier to detect the perturbation signal at higher latitudes than lower. This could partially be due to the difference in perturbation magnitude. The amplitude of the signal peak is two orders of magnitude higher at mid- and high latitudes than at low latitude. If the requirement has been for all perturbations to have the same absolute velocity rather than a percentage of the differential rotation, it is possible that the low-latitude perturbation would be easier to detect.

When the perturbation was increased to 10% of the differential rotation, the increase in velocity resulted in simulation instability (It should be noted that this violation occurred at a perturbation amplitude of 5% for the mid- and high latitude simulations.) The most likely reason that the simulations failed was because the Courant-Friedrichs-Lewy (CFL) condition was defied. This occurs when the velocity exceeds what is physically realizable for the grid space given a particular time discretization.

This does not account for the difference between the mid- and high-latitude 0.01% simulations, however. The high-latitude perturbation can be detected at weaker levels than the mid-latitude perturbation. When the perturbation reaches 0.1%, there are minimal differences between the data sets. It is likely that the lack of obvious signal in the lower amplitude, mid-latitude simulation is due to the baseline simulations already having significant activity at the same latitude. That is, the signal is getting lost in the background noise when it is at the mid-latitude but not the higher latitude where there is not as much activity present in the baseline data.

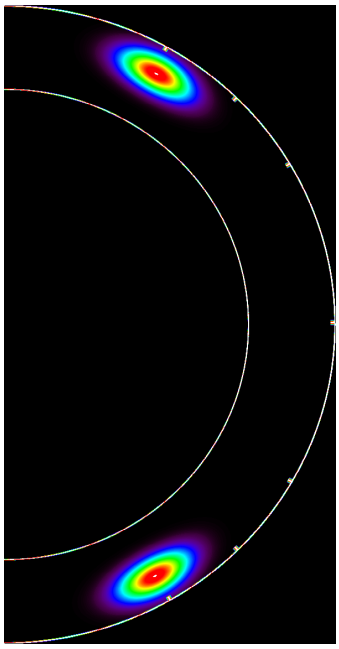

Figure 5.12: High-latitude torsional oscillation distribution

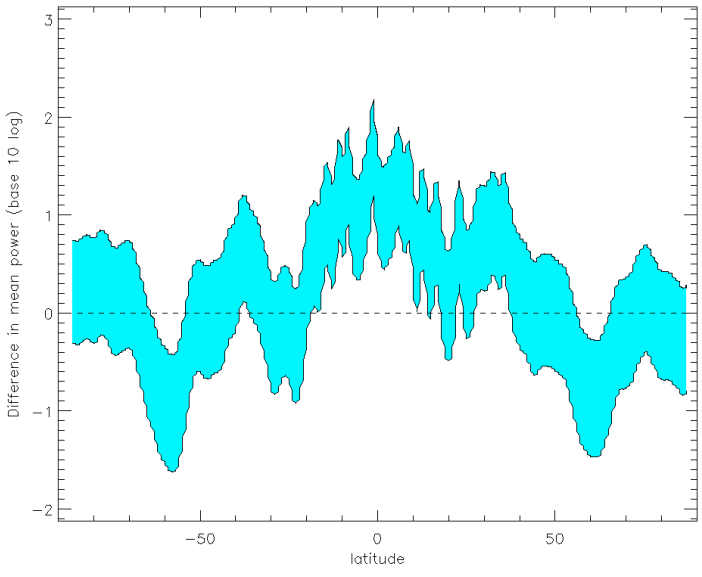

Figure 5.13: High latitude forcing with 0.01% of Ω'

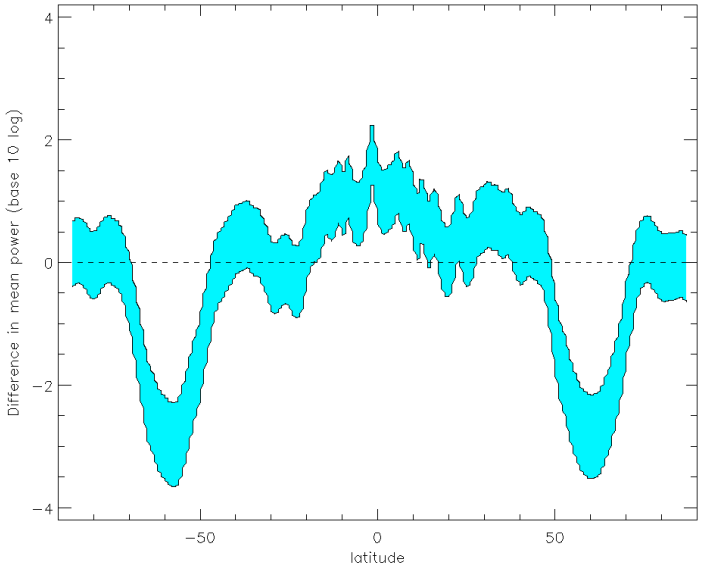

Figure 5.14: High latitude forcing with 0.1% of Ω'

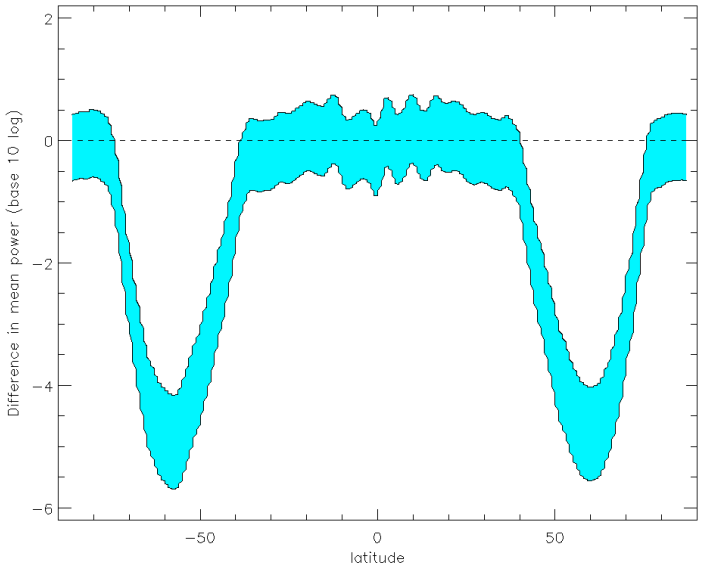

Figure 5.15: High latitude forcing with 1% of Ω'

Chapter 6

Stationary Oscillation Characteristics

6.1 Overview

Stationary perturbations were placed at three different latitudes. Unlike Rempel (2007), no discernible propagation of the signal was detected. There was diffusion and minor distortion on the equatorward portion of the imposed signal. The signal strength did seem to create positive feedback given the power spectra produced by the signals were much larger than expected given the small size of the forcing function amplitude.

6.2 Low-Latitude Results

As discussed in Chapter 3, a perturbation was placed at 30° latitude in each hemisphere. The magnitude of the perturbation was 1% of Ω' and 0.001% of Ω. In Chapter 5, the low-latitude perturbation is shown to have produced a signal that is one order of magnitude greater in power than the ambient.

Figure 6.1 shows a linearly-scaled average of 9 low resolution spectral analyses. The perturbation structure is located in the expected area, though the spatial extent of the signal seems to be slightly reduced from the input signal, which is shown in Chapter 5 Figure 5.4. There continues to be weak frequency content distributed along the bottom and mid-depth of the convection zone, not unlike what was present in the baseline simulations. The peak power value from all simulations is $1.2 \cdot 10^{14}$ which, as expected, is nearly an order of magnitude larger than the peak power value from the baseline simulations, $2.8 \cdot 10^{13}$.

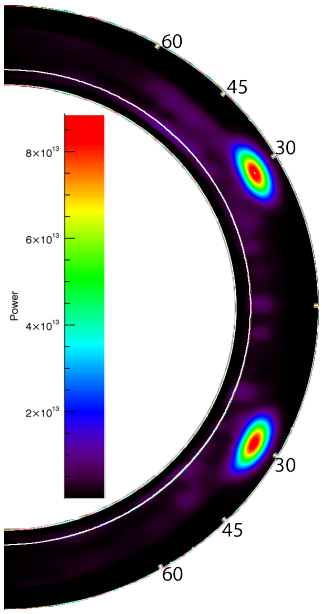

Figure 6.1: Average of low-latitude perturbation spectra

In order to determine the full extent of the perturbation as well as whether it was having an impact on the already existing signal, the data was broken into two parts. The map shown in Figure 6.2 shows the figure scaled to a maximum power of $2.8 \cdot 10^{13}$. This is the same scaling as the baseline progression shown in Chapter 4 Figure 4.1. Any zones that are in white are at or above the maximum value of the baseline simulations.

The signal in both hemispheres has two noticeable areas of distortion. There is a slight elongation of the signal poleward. On the equatorward side of the perturbation, there is a distortion radially inward.

The remaining activity seems to have a similar distribution to the averaged baseline spectra. However, the overall magnitude generally seems to be lower than in the baseline case. In particular, the very active area at the top of the tachocline near 45° has a reduced level of activity compared with the average of the baseline simulations.

The map of values above the baseline maximum is shown in Figure 6.3. The maximum value of the averaged plots is near $8.9 \cdot 10^{13}$. In this figure, we can see that the signal has definitely been attenuated around the edges such that the spatial range of the signal above the baseline is much less than the forcing function.

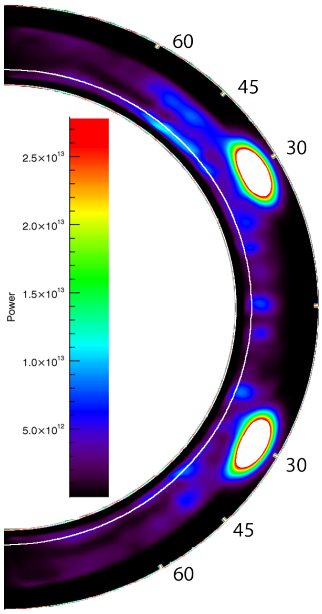

Figure 6.2: Low-latitude average spectrum scaled to a maximum power of $2.8 \cdot 10^{13}$

6.3 Mid-Latitude Results

The mid-latitude simulations place the perturbation at 45°. The average of the spectra, in Figure 6.4, shows that the perturbation appears to span a reduced arc length relative to the forcing function. The peak power value in this average, however, is $1.74 \cdot 10^{17}$, which is four orders of magnitude larger than the max value for the baseline simulations.

When the data is rescaled to the maximum in the baseline value, shown in Figure 6.5, the extent of the perturbation is much larger than in the previous plot. Radially, the signal is present at the top of the convection zone and extends to the top of the tachocline, where it appears to be truncated. The signal also subtends an arc that seems slightly larger than the forcing function. There is distortion near the equatorward portion of the signal along the tachocline: around 45° in both hemispheres, the signal seems to separate from the top of the tachocline. The lower level signal that remains appears to curl under.

The remaining structure outside of the perturbation seems to be slightly altered as the cells equatorward have the appearance of a longer cluster of activity rather than individual cells. There are no obvious differences in poleward activity.

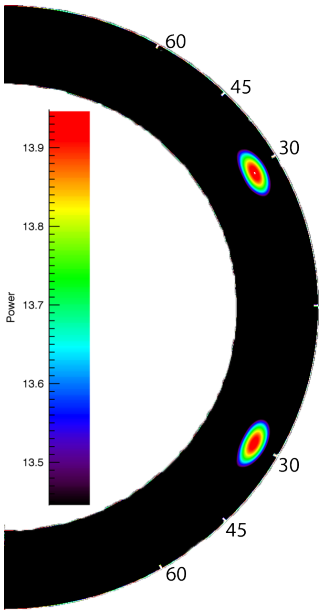

Figure 6.3: Low-latitude average spectrum logarithmically scaled from a minimum of $2.8 \cdot 10^{13}$

Values above baseline maximum are shown in Figure 6.6. The maximum value appears slightly equatorward of 45° and the whole of the signal appears to extend past 30°, unlike the forcing function at this latitude. This indicates that the meridional circulation may be carrying the signal equatorward for a short distance. However, the signal appears to be moved equatorward and distorted rather than propagating. There is also distortion radially inward on the equatorward side of the signals, indicating the flow changes direction there.

6.4 High-Latitude Results

The high-latitude perturbation is shown in Figure 6.7. The peak value for these runs was $3.9 \cdot 10^{17}$. As with the mid-latitude perturbation, the signal seems shifted equatorward of the forcing function, which was centered at 60°. While the distortions seen in the previous results were slight, the central portion of this perturbation has been extended equatorward, likely by the meridional flow in the region.

The scaled spectrum in Figure 6.8 shows that the signal extends to the top of the tachocline. Near 45°, the elongation is present in the perturbation. Radially inward from the elongation, the

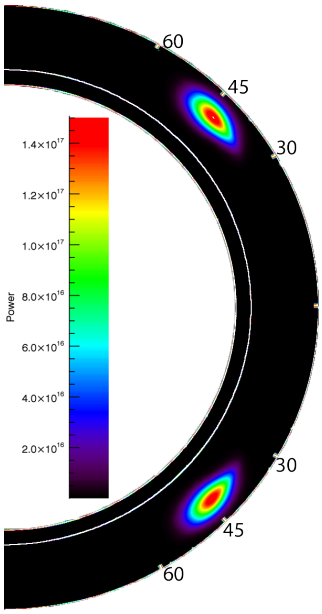

Figure 6.4: Average of mid-latitude perturbation spectra

active cell near the top of the tachocline seems to be present but with reduced intensity. In this case, it is definitely occurring within the tachocline rather than at the base of the convection zone. It also continues to appear in the location of the counter-rotating cell. The activity equatorward of the perturbation again seems to be clustered into individual smaller cells.

The plot of intensities exceeding the baseline minimum is shown in Figure 6.9. In this case, nothing can be seen outside of the perturbation. The shape of the perturbation is to the linearly scaled plot in Figure 6.7. It does, however, have the same extent as was seen in Figure 6.8.

6.5 Discussion

The perturbation does not display the same behavior seen in Rempel (2007): there does not appear to be propagation radially outward and/or toward the equator. The signal seems fairly confined to its origin position, although it is slightly shifted equatorward at higher latitudes. The band of lower-level activity in the outer third of the convection zone does not seem to attenuate the activity of any of the perturbations in a noticeable way. The tachocline and counter-rotating cell near the tachocline at 45° both limit the extent radially inward.

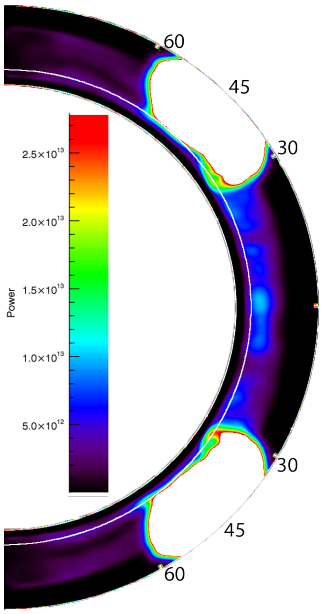

Figure 6.5: Mid-latitude average spectrum scaled to a maximum power of $2.8 \cdot 10^{13}$

Distortion of flow pattern was evident in the mid- and high-latitude simulations more than in the lower latitudes. At middle latitudes, the peak activity within the counter-rotating cell seems to have vorticity. When the perturbation is at high latitudes, it seems to keep the peak activity of the counter-rotating cell confined within the tachocline.

The distortions, however, are somewhat surprising in that they tend to be equatorward. When examining the flows of the model in Rogers paper, the flow direction near the top of the convection zone is poleward. There does not seem to be distortion radially inward where the flow direction has been switched, so it appears that the counter-rotating cell is the most likely candidate to cause the distortions.

The signals at mid- and high latitudes do seem to be diffusing, while the signal at low latitudes appears to be attenuated. This is likely a result of the difference in signal strength at the different latitudes. The mid- and high latitude signal is an order of magnitude or more larger than at low latitudes. This difference is rectified in the moving oscillations shown in the next chapter.

One interesting result of the simulation is that there seems to be some level of positive feedback. In Rempel (2007), the amplitude of the forcing function had to be several percent

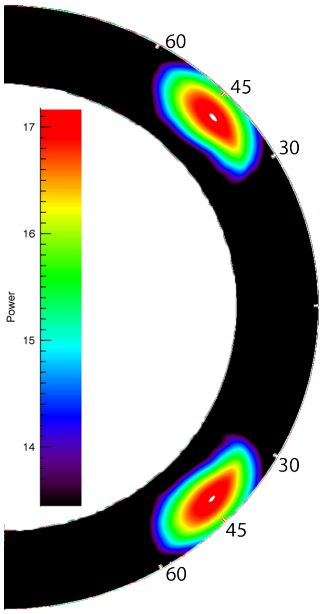

Figure 6.6: Mid-latitude average spectrum logarithmically scaled from a minimum of $2.8 \cdot 10^{13}$

for the signal to noticeable. In these simulations, the amplitude is much smaller yet results in diffusion over a large area. It is large enough to impact the other naturally generated activity found in the baseline simulations, as well. When the simulations were run with larger amplitudes of 5 to 10 times the size shown here, the simulations failed.

Again, the reason this likely occurred was a violation of CFL constraints. While this does point to an issue to be addressed in the future, it does not explain the large spatial extent and magnitude of the signal detected in the spectra. Given such a small signal strength, it is surprising that the frequency content would increase up to four orders of magnitude above the ambient.

Given the presence of naturally occurring activity in the same frequency range, particularly when viewing logarithmic plots of the baseline data, it is possible that there is a natural resonance frequency occurring at the radial level at which the signals have been placed. However, given the attenuation in the outer third of the convection zone, one would expect that the signal would also be attenuated in that region.

Another contributing favor may be that, without a magnetic field, there is nothing to damp the oscillation. This seems somewhat counter-intuitive given the mixing in the convection zone would seem to be sufficient. Initial expectations were that this would be the case and

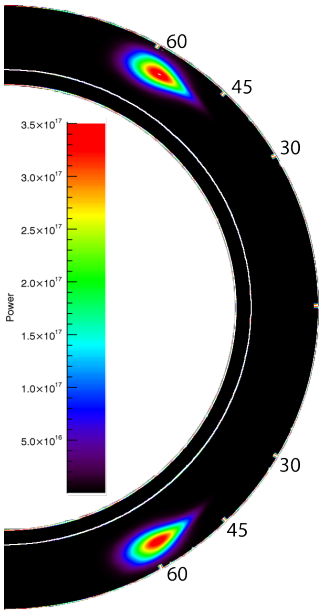

Figure 6.7: Average of high-latitude perturbation spectra

that the convection would actually cause the need for a much larger signal than was used in the simulations. This may indicate that the flow is more coherent than one would expect and that turbulent decay is not carrying sufficient energy away from the perturbation to reduce it's magnitude.

The other issue is why the perturbation doesn't seem to propagate as in Rempel (2007). Unlike Rempel's work, there is no poleward migration of either mid- or high-latitude perturbations. Instead, the simulations show limited mobility of the the signal.

Rempel found that reduced turbulent viscosity increased the propagation time of the signal. It may be that the viscosity used in these simulations was too large for propagation to occur. Given there was virtually no propagation of the signal, it is likely that the forcing did not generate sufficient reduction of density or change in temperature to make the signal buoyant. Another possible solution may be in computational differences regarding the imposition of differential rotation meridional flow patterns. Rempel noted that differing meridional circulation resulted in different propagation behavior. Changing circulation or adding additional constraints on the differential rotation may result in propagation. However, mechanical forcing on its own, in this model, does not seem to result in a propagating signal.

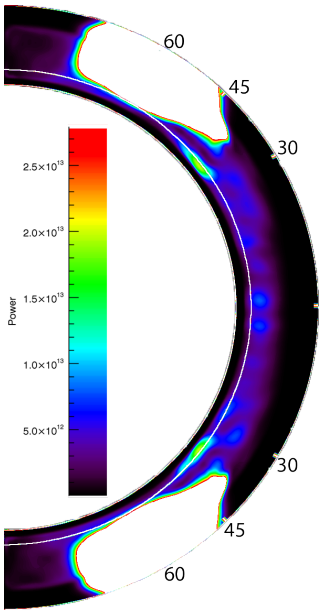

Figure 6.8: High-latitude average spectrum scaled to a maximum power of $2.8 \cdot 10^{13}$

In general, the results differ significantly from Rempel's work. The one behavior that both simulations have in common is that the mechanically forced flows, such as what was modeled here, spread throughout the entire convection zone. Unlike in Rempel's work, however, the forcing did not align with the axis of rotation. This therefore brings up the question whether the Taylor-Proudman condition is insufficient in the simulation given the method of implementation or whether it is a smaller factor than turbulence. In either case, this particular model doesn't require thermal forcing to deviate from Taylor-Proudman.

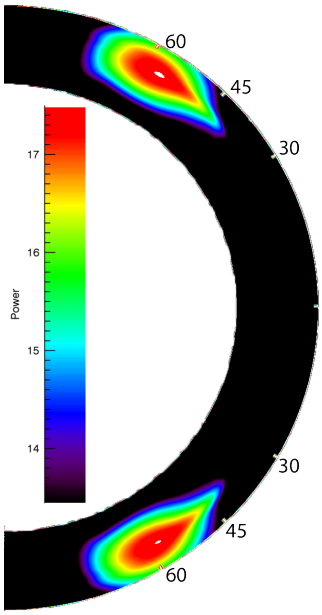

Figure 6.9: High-latitude average spectrum logarithmically scaled from a minimum of $2.8 \cdot 10^{13}$

Chapter 7

Moving Oscillation Characteristics

7.1 Overview

Moving perturbations were injected to determine if the motion had an impact on signal behavior. The signal started at 45° and traveled either poleward or equatorward. The magnitude of the signal strength was constant but the period of motion was 11 years. As before, no propagation was noted. However, the equatorward signal was significantly attenuated for approximately 10° of arc-length around 30° latitude in both hemispheres. There was no attenuation on the poleward signal.

7.2 Poleward

In order to determine if a moving perturbation would accurately replicate some of the characteristics of the torsional oscillation, the forcing function was made to have a variable center that followed an arc while the rest of the forcing function remained the same. In the poleward set of simulations, the perturbation started at 45° and traveled at a constant radial level to approximately 80°. The period of travel was 11 years. The magnitude of the signal was set at 1/10th of the signal used for the stationary perturbation, or 0.1 Ω' at the 45° latitude, because larger magnitudes caused instabilities. The other set of simulations, with the equatorward perturbation traveling from 45° to 10°, will be addressed in the next section.

The poleward propagating average power is shown in Figure 7.1. The maximum power in the poleward perturbations was $1.4 \cdot 10^{15}$, approximately two orders of magnitude larger than

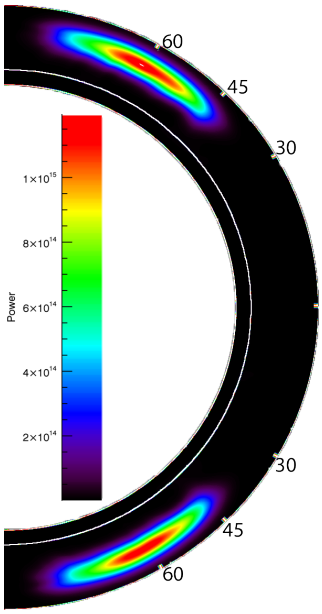

Figure 7.1: Average of poleward perturbation spectra

the baseline maximum.

Like with the stationary oscillations, this map only provides a partial picture, so a linearly scaled plot with a maximum value of $2.8 \cdot 10^{13}$ was generated and is shown in Figure 7.2. The plot shows that the signal again seemed to diffuse outward, though not to the same extent, particularly radially, as the stationary signals. The active region at 45° at the top of the tachocline still seems to have some activity but it is lower in magnitude. There also seems to be some activity near the top of the tachocline at 75° in the northern hemisphere. Unlike stationary simulations, the activity from the equator to 30° in both hemispheres seems to be reduced and is almost inactive.

The logarthimic plot with a minimum of $2.8 \cdot 10^{13}$ is shown in Figure 7.3. The radially inward edge of the perturbation shows some variation, but the map is otherwise fairly unremarkable as it simply shows the signal moving continuously along the radial contour.

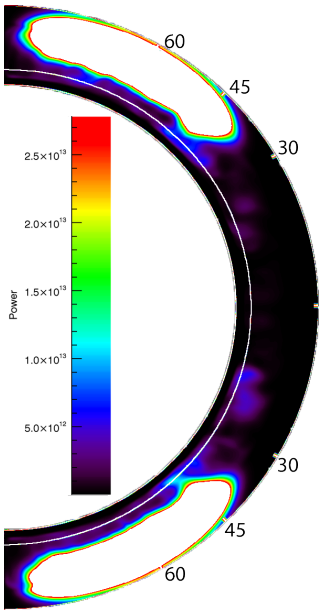

Figure 7.2: Poleward average spectrum scaled to a maximum power of $2.8 \cdot 10^{13}$

7.3 Equatorward

The full results of the the equatorward perturbation are shown in Figure 7.4. The maximum power of the signal is $4.0 \cdot 10^{14}$, only one order of magnitude above the baseline maximimum. The pattern in this map is different than what we would expect as there seems to be an area where the signal is attentuated near 30° in each hemisphere. There are appear to be four indpendent clusters of activity rather than two continuous signals as in the poleward simulations. The attenuated band appears to be about 10° arclength, and the power magnitude drops when the signal resumes closer to the equator.

This same spatial distribution is present in both scaled plots. In Figure 7.6, the logarithmically scaled map is fairly similar to the full-scale map in Figure 7.4. The plot scaled to the maximum of the baseline value, Figure, 7.5, shows some interesting features. In addition to the attenuation at 30°, there are areas of increased activity from the perturbation to the top of the tachocline. These occur at latitudes of approximately 45° and 25° in both hemispheres.

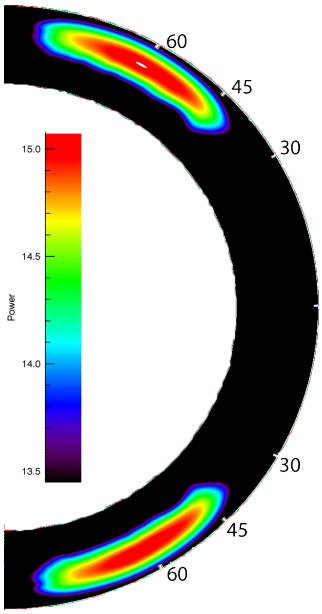

Figure 7.3: Poleward average spectrum scaled logarithmically from a minimum power of $2.8 \cdot 10^{13}$

7.4 Discussion

The results show that adding motion to the perturbation doesn't have a significant impact on the flow pattern. Many of the other characteristics of the stationary perturbations, particularly the appearance of signal diffusion, seem to be similar.

The amplification of the poleward perturbation is half of that seen with the 45° or 60° stationary oscillations. That is, the power maximum was two orders of magnitude larger the baseline maximum instead of four for a reduction in signal amplitude of one order of magnitude. The equatorward signal, however, had the same amplification as the stationary perturbation at 30° despite the reduced forcing attenuation.

In Chapter 4, a map was shown in Figure 4.6 that had been generated from a decimated signal. There were areas of significantly decreased activity at 30° in a band that extended most of the way between the tachocline and the top of the convection zone with some increased activity in the middle portion of the convection zone. Likewise, there are areas of increased activity near the top of the tachocline near 45° and 25° in the equatorward moving signal.

The presence of the gaps in the equatorward perturbation indicates that there is active

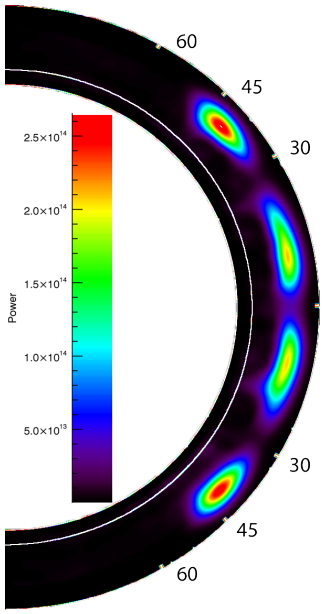

Figure 7.4: Average of equatorward perturbation spectra

attenuation of the signal near 30° and not just lack of presence of a signal. This may be a result of the flow of the counter-rotating cell moving in opposition to other flows or cells that are fairly stable over time. The areas of increased activity in Figure 4.6 may indicate where those cells and flows are occurring.

It is likely that some of this behavior may be reflective of actual convection zone structure. While the counter-rotating cell is fairly small in the these simulations, Zhao et al. (2013) found evidence of a much larger convection cell with this flow direction, giving the meridional circulation a double-cell structure. They did not rule out the possibility that there would be more cells at depth that were not detectable due to limitations of the inversion method.

These results indicate that if this model is an accurate representation of the flow structure in the convection zone, then mechanical forcing of a signal by the magnetic field is not a likely mechanism for a self-sustaining torsional oscillation.

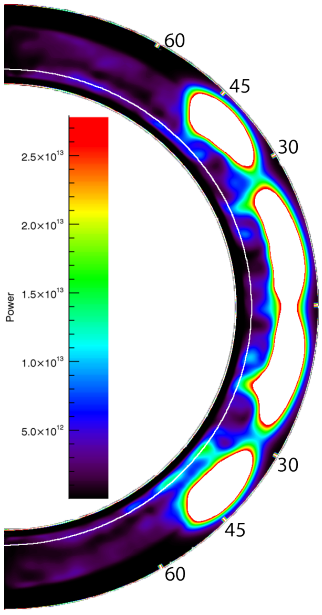

Figure 7.5: Equatorward average spectrum scaled to a maximum power of $2.8 \cdot 10^{13}$

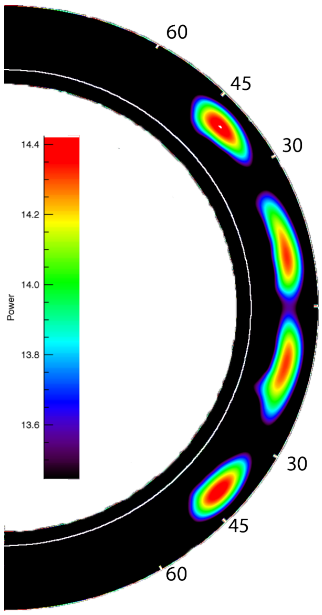

Figure 7.6: Equatorward average spectrum scaled logarithmically from a minimum power of $2.8 \cdot 10^{13}$

Chapter 8

Conclusion

8.1 Summary

This work examined mechanical forcing as a way to emulate the torsional oscillation in the presence of convection.

Initial simulations did not include mechanical forcing as a way to assess baseline conditions. These simulations showed that convection alone could generate a signal at the torsional oscillation frequency. The signal originated near the top of the tachocline at 45° in both hemispheres, likely as a result of the confluence of conditions at the tachocline along with naturally occurring and converging circulation cells and convection currents. This signal seems to change in intensity over time, plausibly making it periodic or pseudoperiodic in nature. However, aside from the possibility of propagating radially outward, the signal shows little latitudinal variation.

The simulations with stationary perturbations showed amplification and diffusion of an imposed mechanical forcing. The results from these simulations, however, contrasted with Rempel's conclusions as they were not constrained by the Taylor-Proudman condition and failed to propagate without forcing.

Finally, moving perturbations also showed amplification of the forcing function and diffusion. The moving signal still seemed to be subject to convection already present as the signal was attenuated at 30°. Areas of high activity seemed to merge with the signal when close enough and extend its spatial range. Active regions not sufficiently close to the signal were often reduced in amplitude.

This work shows that varying some conditions in a solar convection model can have significant changes in the behavior of certain solar features. In particular, some of the conclusions reached in Rempel's work do not seem to be consistent across model approaches and therefore need further study to better constrain the conditions under which torsional oscillation origination and propagation occur.

8.2 Future Work

There are several possibilities to extend this work. Some of them have to do with modifying the model. For instance, one issue that consistently came up was the size of the perturbation causing instability in the program. If the CFL condition was being violated, one correction could be to enlarge the grid size with the assumption that the maximum velocities in each grid space would average out to fall within the CFL constraints. If propagation were to occur, it would be useful to look at the phase instead of solely at amplitude of the signal.

Another possible area to explore would be the reintroduction of a magnetic field. It is possible that the magnetic field would also reduce the instability of the model. Further, it may affect the propagation behavior of the torsional oscillation as well as generate other features or interactions with the torsional oscillation. Further, varying other parameters, such as viscosity, may create variations in these behaviors. It is possible that one or more of these parameters may affect signal amplification, and the mechanism of that amplification should be investigated.

If it can be determined that the naturally occurring signal is likely related to the torsional oscillation, an obvious issue is whether there is a periodicity in its generation. Given the relationship between sunspots and the torsional oscillation, this connection may give some insight to the cause of the grand minima.

Finally, Rempel's work indicates that thermal perturbations may be critical to generating a stable torsional oscillation. This work did not examine thermal perturbations. Modeling thermal perturbations under the same conditions may add additional information about the role of thermal fluctuations.

Bibliography

Basu, S. & Antia, H. 2002, in From Solar Min to Max: Half a Solar Cycle with SOHO, Vol. 508, 59–62

Braginsky, S. I. & Roberts, P. H. 1995, Geophysical and Astrophysical Fluid Dynamics, 79, 1

Bronez, T. P. 1992, IEEE Transactions on Signal Processing, 40, 2941

Howard, R. & LaBonte, B. 1980, The Astrophysical Journal, 239, L33

Howe, R. 2009, Living Reviews in Solar Physics, 6, 1

Howe, R., Christensen-Dalsgaard, J., Hill, F., et al. 2005, The Astrophysical Journal, 634, 1405

Howe, R., Christensen-Dalsgaard, J., Hill, F., et al. 2009, The Astrophysical Journal Letters, 701, L87

Howe, R., Rempel, M., Christensen-Dalsgaard, J., et al. 2006, The Astrophysical Journal, 649, 1155

Prieto, G., Parker, R., & Vernon III, F. 2009, Computers & Geosciences, 35, 1701

Rempel, M. 2005, The Astrophysical Journal, 622, 1320

Rempel, M. 2007, The Astrophysical Journal, 655, 651

Rogers, T. 2011, The Astrophysical Journal, 733, 12

Rogers, T. M. & Glatzmaier, G. A. 2005, The Astrophysical Journal, 620, 432

Thompson, M., Toomre, J., Anderson, E., Antia, H., et al. 1996, Science, 272, 1300

Thomson, D. 1982, Proceedings of the IEEE, 70, 1055

Vorontsov, S., Christensen-Dalsgaard, J., Schou, J., Strakhov, V., & Thompson, M. 2002, Science, 296, 101

Yoshimura, H. 1981, The Astrophysical Journal, 247, 1102

Zhao, J., Bogart, R., Kosovichev, A., Duvall Jr, T., & Hartlep, T. 2013, The Astrophysical Journal Letters, 774, L29